Science Bulletin 64 (2019) 1246–1254

Contents lists available at ScienceDirect

Science Bulletin

journal homepage: www.elsevier.com/locate/scib

Article

A unified poroviscoelastic model with mesoscopic and microscopic heterogeneities

Boya Zhang [a], Dinghui Yang [a,*], Yuanfeng Cheng [b], Yunyin Zhang [b]

[a] Department of Mathematical Sciences, Tsinghua University, Beijing 100084, China
[b] Shengli Geophysical Research Institute of SINOPEC, Dongying 257000, China

ARTICLE INFO

Article history:
Received 10 February 2019
Received in revised form 20 May 2019
Accepted 21 May 2019
Available online 4 June 2019

Keywords:
Mesoscopic heterogeneity
Microscopic heterogeneity
Viscoelastic model
Poroviscoelastic model

ABSTRACT

The wave-induced fluid flow (WIFF) is considered to be the main cause of dispersion and attenuation of seismic waves in fluid-saturated porous media. Among numerous theories, the mesoscopic and microscopic heterogeneities are considered to be the primary mechanisms causing the WIFF. Furthermore, in most rocks, the mesoscopic and microscopic heterogeneities exist simultaneously and can cause obvious transitions of the fast P-wave velocity, which means it is necessary to consider the influence of the two mechanisms on the dispersion and attenuation simultaneously. Numerous results have shown that the dispersions and attenuations caused by these two mechanisms can be approximated in terms of the Zener model. To combine the two mechanisms into a unified model, we introduce a new generalized Zener model into the Biot poroelasticity theory to obtain a new poroviscoelastic model. Comparisons between the numerical results and two groups of experimental data further confirm the validity of our new model.

1. Introduction

As seismic waves carry information about the subsurface characteristics [1,2], the establishment of accurate physical and mathematical models is of great importance to understand the wave propagation in real rocks. An accurate mathematical model is also the basis of seismic modeling and seismic inversion [3,4]. In seismic exploration, the development of models to predict the characteristics of seismic waves in porous media is a considerable challenge. Through numerous experimental progress, the main characteristics of seismic waves are the velocity dispersions and amplitude attenuations, which can be observed in a broad range of frequencies in fluid-saturated porous media [5–8]. Several theories have been proposed to explain these phenomena at various scales [9]. Biot's model is the first model to predict velocity dispersion and amplitude attenuation of seismic waves in fluid-saturated porous media [10–12]. Biot's model provides a macroscopic description of the displacements of the representative volume element (RVE) and a mathematical framework with the Euler-Lagrange equation. With this methodology, the model successfully predicted the existence of the second type compressional wave (the slow P-wave) and has become the foundation of the modern poroelasticity theory. However, Biot's model underestimates the dispersion and attenuation, because it only considers the energy loss of global flow, i.e., the flow caused by the fluid pressure difference at the wavelength scale. In Biot's model, the dissipative force is the frictional force between the matrix and the fluid, which is linear with the relative velocity and is given by the Darcy's law [13].

Following Biot's pioneering work, several other physical mechanisms corresponding to different conditions of rocks and fluids have been proposed [9]. It is now widely accepted that the wave-induced fluid flow (WIFF) is the main cause of energy loss, which leads to dispersion and attenuation of seismic waves. In addition to the Biot global flow mechanism, the mesoscopic heterogeneity [14–17] and the microscopic heterogeneity [18–26] are also the main mechanisms of the WIFF.

The mesoscopic scale is smaller than the seismic wavelength and larger than the grain scale. Pride and Berryman [15,16] developed the double-porosity dual-permeability (DPDP) model describing heterogeneities at the mesoscopic scale. The model assumes that the porous media can be separated into two different phases. The mesoscopic flow from the softer phase to the stiffer phase causes the main energy loss. The effective Biot theory [27] is a simplified case of the DPDP model and assumes that the compliant phase is embedded into the host phase. The effective Biot theory has the same wave equations as Biot's model, but the bulk

* Corresponding author.
E-mail address: ydh@mail.tsinghua.edu.cn (D. Yang).

https://doi.org/10.1016/j.scib.2019.05.027
2095-9273/

modulus of its matrix is frequency-dependent. At high frequency, the fluid pressure caused by the mesoscopic heterogeneity cannot reach the equilibrium condition and the modulus will reach the unrelaxed regime.

At the microscopic scale, the squirt-flow is the main cause of energy dissipation [18–20,23]. The squirt-flow model considers the binary structure of the heterogeneous pore space at the microscopic scale. The compliant pores are mainly cracks with small aspect ratios, and the intergranular pores are stiff with high aspect ratios. The porosities of these two types of pores can be measured under different pressures [8]. Similar to the mesoscopic heterogeneity mechanism, in the high-frequency regime, the fluid in the compliant pores is easily isolated by the stiff pores and the fluid pressure has no time to equilibrate. The rock matrix with fluid in the compliant pores forms a modified matrix [28,29]. In the squirt-flow model of Gurevich et al. [25], the loss mechanism is involved in the frequency-dependent elastic moduli of the modified matrix.

New scanning technology has provided very detailed information on the micro-structure of porous media. Some studied have shown that porous media are likely to be heterogeneous at all scales [30,31]. The dispersions and attenuations caused by mesoscopic and microscopic heterogeneities may appear in different frequency regimes. The frequency at which the velocity transition and attenuation peak appear is called the characteristic frequency [32]. The characteristic frequencies of the mesoscopic and the microscopic heterogeneities depend on rock properties, fluids, and pore geometries [32]. Pimienta et al. [33] reported that Young's modulus and Poisson's ratio of a fully-saturated tight Wilkenson sandstone exhibited two transitions and two attenuation peaks. Using a numerical oscillatory compressibility test, Rubino and Holliger [34] obtained the dispersion and attenuation curves of the fast P-waves in a medium containing heterogeneities at two scales. The dispersion curve has two transitions and the attenuation curve has two peaks. Therefore, it is necessary to propose a mathematical model that can describe both mechanisms simultaneously. Bachrach [35] proposed a model combining the mesoscopic heterogeneity of the patchy saturation and microscopic heterogeneity. However, the model cannot describe the mesoscopic heterogeneity of the rock fabric. We aim to develop a model with a broad scope of applications, i.e., a model capable of describing the two mesoscopic heterogeneities of rock fabric and patchy saturation. In this study, we use the poroviscoelastic theory to establish a unified model that includes the heterogeneities at the microscopic and mesoscopic scales and is presented in time and frequency domains.

The concept of the poroviscoelastic theory is to replace the elastic moduli in Biot's theory by the viscoelastic moduli [36]. Carcione [36] used the viscoelastic moduli of the Zener model (or standard linear solid) [37] to replace the elastic moduli in Biot's model and provided wave equations with relaxation functions in the time domain. The Carcione poroviscoelastic model [36] has one more velocity transition and one more attenuation peak than Biot's model. The new transition and peak are located at the characteristic frequency of the Zener model. In our present study, we use a new generalized Zener model to describe the two transitions and three regimes in the dispersion curve caused by the mesoscopic and microscopic heterogeneities. The traditional generalized Zener model is a parallel connection of several Zener solids [13]. Liu et al. [38] substituted the moduli of the traditional generalized Zener model for the effective elastic moduli in the effective Biot theory. However, it is difficult to analytically determine the viscoelastic parameters in the traditional generalized Zener model. Liu et al. [38] determined the viscoelastic parameters by the optimal methods with known attenuation information. In our new generalized Zener model, all the parameters can be determined by the two types of heterogeneity without the use of dispersion or attenuation information.

2. Dispersions and attenuations caused by the WIFF

2.1. Heterogeneities at mesoscopic and microscopic scales

There are mainly two causes of mesoscopic heterogeneities: the first one is the heterogeneity of rock fabric [15,17]. Because rocks consist of different types of mineral granules, different parts of the rock fabric may have different elastic and hydraulic properties. For example, many sandstones contain a portion of clay, which is softer than other mineral granules and has smaller elastic moduli, larger porosity, and larger permeability. When a compressional wave squeezes the RVE, the clay phase is compressed to a greater degree and fluid in the clay phase will squirt into the stiff phase, causing energy dissipation. This phenomenon is called the clay squirt flow [39,40]. The second cause is the patchy saturation of immiscible fluids [14,41]. Similar to the mesoscopic heterogeneity in the rock fabric, the elasticity difference of the immiscible fluids also causes strong energy dissipation. White [14] and Johnson [41] suggested models to describe the energy dissipation caused by the patchy saturation of immiscible fluids. Ba et al. [42] introduced a new model to describe these two kinds of mesoscopic heterogeneities simultaneously.

The microscopic scale is the scale of the pores, throats, and mineral granules. The WIFF at the microscopic scale is known as the squirt-flow [25]. The pressure difference at the microscopic scale is induced by the compressibility difference between two pore types. Pores can be classified into stiff pores (with porosity ϕ_p) and compliant pores (with porosity ϕ_c). The squirt-flow mechanism explains the effects of low frequency and high frequency on fluid. If the frequency is much higher than the characteristic frequency, the pressure cannot equilibrate in one period of wave propagation. The compliant pores are isolated by stiff pores and can be treated as part of the matrix [28].

Several experiments have been conducted to characterize the dispersion and attenuation of waves caused by the WIFF [5,8,33,43–47]. In the low- and high-frequency regimes, the velocity and the elastic moduli are nearly constants. The obvious velocity transition appears around the characteristic frequency. The causality between dispersion and attenuation is described by the Kramers-Kronig relationship [48]. Attenuation is quantified by the inverse quality factor and its peak also appears at the characteristic frequencies. Experimental data [33,43–47] have shown that dispersion and attenuation can be approximated by the Zener model [37] or the Cole-Cole model [49]. Both models are viscoelastic models and have the same characteristics of dispersion and attenuation as the experimental data. The dispersions of the two models have low- and high-frequency limits and the transition regimes around the characteristic frequencies. The attenuations of the two models have peaks at the characteristic frequencies. The differences between the two models are the transition widths of the dispersions and the asymptotic behavior of the attenuations.

2.2. The Zener model

The Zener model has a complex modulus [13] as

$$Z(\omega) = Z_R \frac{1 + i\omega\tau_\varepsilon}{1 + i\omega\tau_\sigma}, \tag{1}$$

where τ_σ and τ_ε are the relaxation times of stress and strain, respectively. i is the imaginary unit and Z_R is the low-frequency limit modulus of complete relaxation, i.e., the relaxed modulus. The unrelaxed modulus is defined by

$$Z_U := \lim_{\omega\to\infty} Z(\omega) = Z_R \frac{\tau_\varepsilon}{\tau_\sigma}. \tag{2}$$

Following the definition of the inverse quality factor $Q^{-1} = \mathrm{Im}(Z)/\mathrm{Re}(Z)$ [13], the inverse quality factor of the Zener model is

$$Q^{-1} = \frac{\omega(\tau_\varepsilon - \tau_\sigma)}{1 + \omega^2\tau_\varepsilon\tau_\sigma}, \tag{3}$$

which has a peak denoted as [13]

$$\left(\omega_0, Q_0^{-1}\right) = \left(\frac{1}{\sqrt{\tau_\varepsilon\tau_\sigma}}, \frac{\tau_\varepsilon - \tau_\sigma}{2\sqrt{\tau_\varepsilon\tau_\sigma}}\right). \tag{4}$$

From Eqs. (2) and (4), we can obtain τ_σ and τ_ε in terms of the relaxed modulus Z_R, the unrelaxed modulus Z_U, and the characteristic frequency ω_0:

$$\tau_\varepsilon = \frac{1}{\omega_0}\sqrt{\frac{Z_U}{Z_R}}, \tau_\sigma = \frac{1}{\omega_0}\sqrt{\frac{Z_R}{Z_U}}. \tag{5}$$

Substituting Eq. (5) into Eq. (1), we have

$$Z(\omega) = Z_R \frac{1 + \mathrm{i}\frac{\omega}{\omega_0}\sqrt{\frac{Z_U}{Z_R}}}{1 + \mathrm{i}\frac{\omega}{\omega_0}\sqrt{\frac{Z_R}{Z_U}}}. \tag{6}$$

From the three viscoelastic parameters Z_R, Z_U, and ω_0, we can obtain the dispersion and attenuation in the entire frequency range.

3. A new poroviscoelastic model that includes the mesoscopic and microscopic heterogeneities

3.1. A new viscoelastic modulus

The traditional generalized Zener model is a parallel combination of several Zener solids [13]. The expression of its complex modulus is given by

$$Z(\omega) = \sum_{k=1}^{K} Z_{Rk} \frac{1 + \mathrm{i}\omega\tau_{\varepsilon k}}{1 + \mathrm{i}\omega\tau_{\sigma k}}. \tag{7}$$

In some previous studies [38,50], attenuation data were used to obtain the viscoelastic parameters by the optimal method. However, this kind of implementation is independent of the mechanisms and cannot obtain the analytic expressions of viscoelastic parameters. Therefore, we suggest a new viscoelastic model in this study, in which all parameters are determined analytically based on the heterogeneity mechanisms and are independently measurable.

As shown in Fig. 1, to describe the dispersion and attenuation of waves in a broad frequency range, we need to determine the types of the two modulus transitions and the viscoelastic parameters. The experimental results [5,44,51] have shown that the transitions of velocity and elastic moduli can be approximated by the Zener model. We need a new viscoelastic modulus that contains two transitions of Zener type. The modulus of the Zener model can be regarded as the relaxed modulus multiplied by a multiplier. This multiplier is approximately equal to 1 when the frequency is much lower than the characteristic frequency and it is approximately equal to Z_U/Z_R when the frequency is much higher than the characteristic frequency, which implies that the viscoelastic modulus is approximately equal to the unrelaxed modulus in the high-frequency regime. Around the characteristic frequency, the multiplier includes the transition process of the Zener model. To develop the new viscoelastic modulus with two Zener type transitions, we multiply two multipliers by the relaxed modulus. The new viscoelastic modulus with the two Zener type transitions is defined by:

$$Z(\omega) = Z_R \frac{\left(1 + \mathrm{i}\frac{\omega}{\omega_1}\sqrt{\frac{Z_M}{Z_R}}\right)}{\left(1 + \mathrm{i}\frac{\omega}{\omega_1}\sqrt{\frac{Z_R}{Z_M}}\right)} \cdot \frac{\left(1 + \mathrm{i}\frac{\omega}{\omega_2}\sqrt{\frac{Z_U}{Z_M}}\right)}{\left(1 + \mathrm{i}\frac{\omega}{\omega_2}\sqrt{\frac{Z_M}{Z_U}}\right)}, \tag{8}$$

where ω_1 and ω_2 are the two characteristic frequencies. Z_M is the partial-unrelaxed modulus and corresponds to the modulus of regime 2 in Fig. 1.

When the frequency is much smaller than the second characteristic frequency, i.e., $\omega \ll \omega_2$, the modulus $Z(\omega)$ is approximately written as

$$Z(\omega \ll \omega_2) = Z_R \frac{\left(1 + \mathrm{i}\frac{\omega}{\omega_1}\sqrt{\frac{Z_M}{Z_R}}\right)}{\left(1 + \mathrm{i}\frac{\omega}{\omega_1}\sqrt{\frac{Z_R}{Z_M}}\right)}. \tag{9}$$

This is the same as the Zener model and represents the first transition in the dispersion curve. Similarly, when the frequency is much larger than the first characteristic frequency, i.e., $\omega \gg \omega_1$, the modulus degenerates to another Zener model, representing the second transition in the dispersion curve:

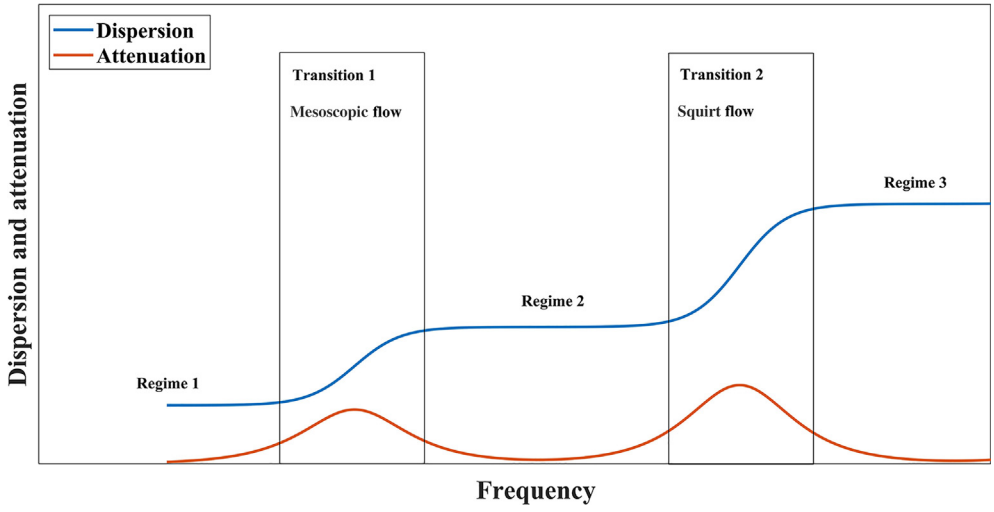

Fig. 1. The sketch of dispersion and attenuation caused by the mesoscopic and microscopic heterogeneities. The two transitions and two peaks are caused by the two main mechanisms, respectively.

$$Z(\omega \gg \omega_1) = Z_M \frac{\left(1 + i\frac{\omega}{\omega_2}\sqrt{\frac{Z_U}{Z_M}}\right)}{\left(1 + i\frac{\omega}{\omega_2}\sqrt{\frac{Z_M}{Z_U}}\right)}. \quad (10)$$

The two transitions of the new viscoelastic model are both Zener type transitions, satisfying the transition characteristics of the dispersion, as shown in Fig. 1. When one energy loss mechanism is neglected, i.e., $Z_R = Z_M$ or $Z_M = Z_U$, the new viscoelastic modulus will degenerate to the Zener model as described in Eq. (1).

3.2. Determination of the viscoelastic parameters

In the last section, we have introduced a new viscoelastic model containing two Zener type transitions. In this section, we will apply the new viscoelastic model to the porous media with mesoscopic and microscopic heterogeneities and determine the analytic expressions of the viscoelastic parameters. As mentioned in Section 2, fluid pressure cannot reach the equilibrium condition when the frequency is higher than the characteristic frequency. The isolated part of fluid can be regarded as a portion of the effective matrix. The moduli of the effective matrix consisting of solid and isolated fluid can be regarded as the viscoelastic moduli. We can replace the bulk modulus K_m by a new viscoelastic bulk modulus $K_{unified}$ in the poroelasticity theory. The two transitions of $K_{unified}$ are caused by the mesoscopic and microscopic heterogeneities, respectively. By applying the new viscoelastic model to modulus $K_{unified}$, we can obtain

$$K_{unified}(\omega) = K_m \frac{\left(1 + i\frac{\omega}{\omega_{meso}}\sqrt{\frac{K^{ur}_{meso}}{K_m}}\right)}{\left(1 + i\frac{\omega}{\omega_{meso}}\sqrt{\frac{K_m}{K^{ur}_{meso}}}\right)} \cdot \frac{\left(1 + i\frac{\omega}{\omega_{micro}}\sqrt{\frac{K^{ur}_{micro}}{K^{ur}_{meso}}}\right)}{\left(1 + i\frac{\omega}{\omega_{micro}}\sqrt{\frac{K^{ur}_{meso}}{K^{ur}_{micro}}}\right)}. \quad (11)$$

There are five viscoelastic parameters in the new viscoelastic modulus that need to be determined, including the values in the three regimes of Fig. 1 and the two characteristic frequencies. ω_{meso} and ω_{micro} are the two characteristic frequencies of $K_{unified}$ and they correspond to the characteristic frequencies of the two mechanisms. The expressions of the characteristic frequencies are provided by Pride et al. [52] and Jones [53], respectively:

$$\omega_{meso} = 2\pi \frac{M\kappa}{L^2\eta}, \quad (12)$$

$$\omega_{micro} = 2\pi \frac{\alpha_m^3 K_s}{\eta}, \quad (13)$$

where L is the scale of the mesoscopic heterogeneity and α_m is the average aspect ratio of the pores. η is the viscosity of fluid and κ is permeability. K_s is the bulk modulus of solid mineral. M is the fluid storage coefficient [54], whose expression will be described in the next section.

The moduli in the three regimes correspond to the relaxed modulus, the unrelaxed modulus of the mesoscopic heterogeneity K^{ur}_{meso}, and the unrelaxed modulus of the microscopic heterogeneity K^{ur}_{micro}. The relaxed modulus of $K_{unified}$ is the static matrix bulk modulus K_m. For typical properties of tight porous rocks [8], we can confirm that the characteristic frequency of the mesoscopic heterogeneity is lower than the characteristic frequency of the microscopic heterogeneity, so we regard the unrelaxed modulus of the mesoscopic heterogeneity as the partially unrelaxed modulus in this work. In regime 2 of Fig. 1, part of the fluid is isolated and reaches the unrelaxed state, as a result of the mesoscopic heterogeneity. Whereas some more fluid reaches the unrelaxed state when the frequency reaches regime 3 of Fig. 1 and the modulus in the third regime corresponds to the unrelaxed modulus of the microscopic heterogeneity.

The unrelaxed modulus of the mesoscopic heterogeneity is provided by the DPDP model [15,16,27]:

$$K^{ur}_{meso} = K_m \frac{a_{33}}{a_{33} - a_{13}^2 K_m}, \quad (14)$$

where a_{13} and a_{33} are coefficients in the constitutive relationship of the DPDP model. The governing dynamic equations of the DPDP model are based on Biot's poroelasticity theory with an additional transport equation that describes the internal mesoscopic flow [15,16]. We present the governing dynamic equations of the DPDP model in Appendix A.

The unrelaxed modulus of the microscopic heterogeneity is provided by Gurevich et al. [25]:

$$K^{ur}_{micro} = K_h, \quad (15)$$

where K_h is the matrix bulk modulus of a hypothetical medium without compliant pores. The derivation of the unrelaxed modulus of the microscopic heterogeneity is presented in Appendix B, online.

By now, we have provided the method to determine the parameters of the viscoelastic matrix bulk modulus. The new viscoelastic model has two Zener type transitions, corresponding to two energy loss mechanisms, respectively. We can generalized the model by multiplying more Zener type multipliers with the static modulus to add more modulus transitions and more attenuation peaks. The viscoelastic modulus has the following form:

$$Z(\omega) = Z_1 \frac{\left(1 + i\frac{\omega}{\omega_1}\sqrt{\frac{Z_2}{Z_1}}\right)}{\left(1 + i\frac{\omega}{\omega_1}\sqrt{\frac{Z_1}{Z_2}}\right)} \cdot \frac{\left(1 + i\frac{\omega}{\omega_2}\sqrt{\frac{Z_3}{Z_2}}\right)}{\left(1 + i\frac{\omega}{\omega_2}\sqrt{\frac{Z_2}{Z_3}}\right)} \cdot \ldots \cdot \frac{\left(1 + i\frac{\omega}{\omega_{n-1}}\sqrt{\frac{Z_n}{Z_{n-1}}}\right)}{\left(1 + i\frac{\omega}{\omega_{n-1}}\sqrt{\frac{Z_{n-1}}{Z_n}}\right)}, \quad (16)$$

where $Z_1, Z_2, \ldots Z_n$ are the moduli in different regimes of the frequency domain, and $\omega_1, \omega_2, \ldots, \omega_{n-1}$ are the characteristic frequencies of the mechanisms.

If other mechanisms are involved, we can also use other viscoelastic models as substitutions. For example, Picotti and Carcione [55] used the Cole-Cole model to approximate White's model and Johnson's model. We can use the Cole-Cole model to replace the Zener model in Eq. (16), when considering the case including White's or Johnson's models.

3.3. A new poroviscoelastic model

The poroviscoelastic model suggested by Carcione [36] introduces the viscoelastic moduli into Biot's poroelasticity theory. The dynamic equations of the porous continuum are given by [10,12]:

$$\nabla \cdot \boldsymbol{\tau}^D - \nabla p_c = \rho \ddot{\boldsymbol{u}} + \rho_f \ddot{\boldsymbol{w}}, \quad (17)$$

$$-\nabla p_f = \frac{\eta}{\kappa}\dot{\boldsymbol{w}} + \rho_f \ddot{\boldsymbol{u}} + t_m \rho_f \ddot{\boldsymbol{w}}, \quad (18)$$

where $\boldsymbol{u}$ is the displacement vector of the solid. $\boldsymbol{w}$ represents the flow of the fluid relative to the solid and is defined as $\boldsymbol{w} = \phi(\boldsymbol{U} - \boldsymbol{u})$, where $\boldsymbol{U}$ is the displacement vector of the fluid. The dots above $\boldsymbol{u}$ and $\boldsymbol{w}$ denote time differentiations. $p_c = -\mathrm{tr}(\boldsymbol{\tau})/3$, p_f, and $\boldsymbol{\tau}^D = \boldsymbol{\tau} + p_c\mathbf{I}$ are the confining pressure, pore pressure, and deviatoric stress tensor, respectively, where $\boldsymbol{\tau}$ is the stress tensor of the RVE and $\mathbf{I}$ is the identity matrix. $\rho = (1-\phi)\rho_s + \phi\rho_f$ is the density of the RVE, where ρ_s and ρ_f are the densities of the solid grain and the fluid, respectively, and ϕ is the porosity. Eq. (17) is the equation of motion of RVE and Eq. (18) is the effective Darcy's law, with permeability κ and fluid viscosity η. t_m is the tortuosity of the porous medium. Substituting the constitutive relationship of the RVE [12]:

$$\tau_{jk} = (K_G e - \frac{2}{3}\mu e + \alpha M \xi)\delta_{jk} + 2\mu e_{jk}, \quad (19)$$

$$p_f = -\alpha M e - M\xi, \tag{20}$$

into Eqs. (17) and (18), we can obtain the final form:

$$\mu\nabla^2\boldsymbol{u} + \left(\frac{1}{3}\mu + K_G\right)\nabla e + \alpha M\nabla\xi = \rho\ddot{\boldsymbol{u}} + \rho_f\ddot{\boldsymbol{w}}, \tag{21}$$

$$\nabla(\alpha M e + M\xi) = (\rho_f\ddot{\boldsymbol{u}} + t_m\rho_f\ddot{\boldsymbol{w}}) + \frac{\eta}{\kappa}\dot{\boldsymbol{w}}. \tag{22}$$

In the constitutive relationship, $e_{jk} = \frac{1}{2}\left(\frac{\partial u_j}{\partial x_k} + \frac{\partial u_k}{\partial x_j}\right)$ and $\xi_{jk} = \frac{1}{2}\left(\frac{\partial w_j}{\partial x_k} + \frac{\partial w_k}{\partial x_j}\right)$ are the strain components, where $j,k = 1,2,3$. The dilatations are defined as $e = e_{jj}$ and $\xi = \xi_{jj}$ (the Einstein summation for repeated index is implied unless stated otherwise). δ_{jk} is the Kronecker delta function. The Biot-Willis coefficient α and the fluid storage coefficient M are functions of the bulk moduli of the solid grain, K_s, the fluid, K_f, and the solid matrix, K_m:

$$\alpha = 1 - K_m/K_s, \tag{23}$$

$$M = (\phi/K_f + (\alpha - \phi)/K_s)^{-1}. \tag{24}$$

And

$$K_G = K_m + \alpha^2 M \tag{25}$$

is the Gassmann bulk modulus. μ is the shear modulus of rock matrix.

Eqs. (23)–(25) show that α, M, and K_G are dependent on the matrix bulk modulus. Therefore, to develop the poroviscoelastic model containing two heterogeneity mechanisms, we need to substitute the new viscoelastic modulus $K_{unified}$ for the elastic modulus K_m in Eqs. (23)–(25). The frequency-dependent coefficients are denoted as $\bar{\alpha}$, $\bar{M}$, and $\bar{K_G}$. The wave equations in the frequency domain are as follows:

$$\bar{\mu}\nabla^2\boldsymbol{u} + \left(\frac{1}{3}\bar{\mu} + \bar{K_G}\right)\nabla e + \bar{\alpha}\bar{M}\nabla\xi = -\omega^2\rho\boldsymbol{u} - \omega^2\rho_f\boldsymbol{w}, \tag{26}$$

$$\nabla\left(\bar{\alpha}\bar{M}e + \bar{M}\xi\right) = -\omega^2(\rho_f\boldsymbol{u} + t_m\rho_f\boldsymbol{w}) + i\omega\frac{\eta}{\kappa}\boldsymbol{w}. \tag{27}$$

Here we also replace the shear modulus μ by a new notation $\bar{\mu}$ because the shear modulus is also frequency-dependent in heterogeneous media [25,27]. We use the expression of the shear modulus given by Gurevich et al. [25] in the following sections.

3.4. Constitutive relationship of the new generalized Zener model

To obtain the equation in the time domain, we need to apply the single phase viscoelastic model to obtain the relaxation function. The traditional viscoelasticity theory is based on mechanical models, assuming that the viscoelastic element is combined by springs and dashpots with constitutive relationships of elastic bodies and Newtonian fluids, respectively. The constitutive relationship of the viscoelastic element can be obtained by series and parallel connections [13]. The new generalized Zener model can also be represented by a mechanical model. Its mechanical representation is a series connection of the Zener model and the Kelvin model as shown in Fig. 2. The constitutive relationships of the springs and dashpots are as follows:

$$\sigma = k_1\varepsilon_1, \tag{28a}$$

$$\sigma_1 = k_2\varepsilon_2, \tag{28b}$$

$$\sigma_2 = \eta_2\partial_t\varepsilon_2, \tag{28c}$$

$$\sigma_3 = k_3\varepsilon_3, \tag{28d}$$

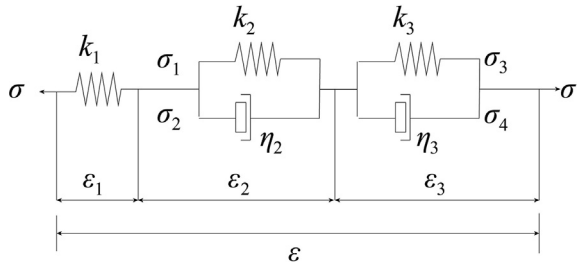

Fig. 2. The mechanical representation of the new viscoelastic model. It is equivalent to a series connection of a Zener solid and a Kelvin-Voigt solid.

$$\sigma_4 = \eta_3\partial_t\varepsilon_3, \tag{28e}$$

where k_1, k_2, and k_3 are the elastic moduli of the springs and η_1, η_2 are the viscosities of the dashpots. The constitutive relationship of the whole viscoelastic element satisfies the basic principles of the series and parallel connection connections. The total stress is equal to the sum of the parallel stress, while the total strain is equal to the sum of the series connection strain [13]:

$$\sigma = \sigma_1 + \sigma_2 = \sigma_3 + \sigma_4, \tag{29a}$$

$$\varepsilon = \varepsilon_1 + \varepsilon_2 + \varepsilon_3. \tag{29b}$$

By substituting Eqs. (28a)–(28e) into Eqs. (29a) and (29b), we obtain the following differential equation describing the total stress and total strain:

$$\begin{aligned}&(k_2 + \eta_2\partial_t)(k_3 + \eta_3\partial_t)\sigma + k_1(k_2 + \eta_2\partial_t)\sigma + k_1(k_3 + \eta_3\partial_t)\sigma\\ &= k_1(k_2 + \eta_2\partial_t)(k_3 + \eta_3\partial_t)\varepsilon.\end{aligned} \tag{30}$$

By applying a Fourier transform to Eq. (30), we can obtain the frequency-domain equation as follows:

$$(1 + i\omega\tau_{\sigma1})(1 + i\omega\tau_{\sigma2})\sigma = Z_R(1 + i\omega\tau_{\varepsilon1})(1 + i\omega\tau_{\varepsilon2})\varepsilon, \tag{31}$$

with the following expressions of the relaxed modulus and relaxation times:

$$Z_R = \frac{k_1k_2k_3}{k_1k_2 + k_2k_3 + k_1k_3}, \tag{32a}$$

$$\tau_{\varepsilon1} = \frac{\eta_2}{k_2}, \tag{32b}$$

$$\tau_{\varepsilon2} = \frac{\eta_3}{k_3}, \tag{32c}$$

$$\tau_{\sigma1} = \frac{(k_1 + k_3)\eta_2}{k_1k_2 + k_2k_3 + k_1k_3}, \tag{32d}$$

$$\tau_{\sigma2} = \frac{(k_1 + k_2)\eta_3}{k_1k_2 + k_2k_3 + k_1k_3}. \tag{32e}$$

Eq. (31) can further be rewritten as

$$\sigma = Z_R\frac{(1 + i\omega\tau_{\varepsilon1})(1 + i\omega\tau_{\varepsilon2})}{(1 + i\omega\tau_{\sigma1})(1 + i\omega\tau_{\sigma2})}\varepsilon, \tag{33}$$

the viscoelastic modulus is $Z_R\frac{(1+i\omega\tau_{\varepsilon1})(1+i\omega\tau_{\varepsilon2})}{(1+i\omega\tau_{\sigma1})(1+i\omega\tau_{\sigma2})}$. Although we have established the model using mechanical models, we cannot provide the elastic moduli of the springs and the viscosities of the dashpots because they are abstract parameters. We have to apply the energy loss mechanisms to determine the parameters. The relaxation times in Eq. (33) can be obtained by comparing the viscoelastic modulus with Eq. (8):

$$\tau_{\varepsilon1} = \frac{1}{\omega_1}\sqrt{\frac{Z_M}{Z_R}}, \tag{34a}$$

$$\tau_{\sigma 1} = \frac{1}{\omega_1}\sqrt{\frac{Z_R}{Z_M}}, \tag{34b}$$

$$\tau_{\varepsilon 2} = \frac{1}{\omega_2}\sqrt{\frac{Z_U}{Z_M}}, \tag{34c}$$

$$\tau_{\sigma 2} = \frac{1}{\omega_2}\sqrt{\frac{Z_M}{Z_U}}. \tag{34d}$$

In the time domain, the constitutive relationship is written in the form [13]:

$$\sigma = \psi(t) * \partial_t \varepsilon \text{ or } \varepsilon = \chi(t) * \partial_t \sigma, \tag{35}$$

where $\psi(t)$ and $\chi(t)$ are the relaxation and creep functions, respectively, and "*" denotes convolution. From Eqs. (30) and (31), we can write the constitutive relationship as follows:

$$\varepsilon = \frac{\sigma}{k_1} + \frac{\sigma}{k_2 + i\omega\eta_2} + \frac{\sigma}{k_3 + i\omega\eta_3} = J(\omega)\sigma, \tag{36}$$

where

$$J(\omega) = \frac{1}{Z(\omega)} = \frac{1}{k_1} + \frac{1}{k_2 + i\omega\eta_2} + \frac{1}{k_3 + i\omega\eta_3} \tag{37}$$

is the complex creep compliance of the model. The creep function is the inverse Fourier transform of the creep compliance:

$$\begin{aligned}\chi(t) &= \left\{\frac{1}{k_1} + \frac{1}{k_2}[1 - \exp(-t/\tau_{\varepsilon 1})] + \frac{1}{k_3}[1 - \exp(-t/\tau_{\varepsilon 2})]\right\}H(t) \\ &= \frac{1}{Z_R}\left[1 - \left(1 - \frac{\tau_{\sigma 1}}{\tau_{\varepsilon 1}}\right)\exp(-t/\tau_{\varepsilon 1}) - \left(1 - \frac{\tau_{\sigma 2}}{\tau_{\varepsilon 2}}\right)\exp(-t/\tau_{\varepsilon 2})\right]H(t),\end{aligned} \tag{38}$$

where $H(t)$ is the Heaviside or step function. Since the stress-strain relationship in Eq. (31) is symmetric, we only need to substitute Z_R for $1/Z_R$ and exchange the role of $\tau_{\varepsilon 1}$ and $\tau_{\sigma 1}$, $\tau_{\varepsilon 2}$ and $\tau_{\sigma 2}$, respectively. Then the relaxation function can be written as

$$\psi(t) = Z_R\left[1 - \left(1 - \frac{\tau_{\varepsilon 1}}{\tau_{\sigma 1}}\right)\exp(-t/\tau_{\sigma 1}) - \left(1 - \frac{\tau_{\varepsilon 2}}{\tau_{\sigma 2}}\right)\exp(-t/\tau_{\sigma 2})\right]H(t). \tag{39}$$

Following Ref. [56], to obtain the wave equations in the time domain, each product between the viscoelastic modulus and strain in Eqs. (26) and (27) needs to be replaced by the convolution between the relaxation function and the strain rate. Then we can obtain the poroviscoelastic wave equations in the time domain:

$$\psi_\mu * \nabla^2 \dot{\boldsymbol{u}} + \left(\frac{1}{3}\psi_\mu + \psi_{K_G}\right) * \nabla\dot{e} - \psi_{\alpha M} * \nabla\dot{\zeta} = \rho\ddot{\boldsymbol{u}} + \rho_f\ddot{\boldsymbol{w}}, \tag{40a}$$

$$\psi_{\alpha M} * \nabla\dot{e} - \psi_M * \nabla\dot{\zeta} = (\rho_f\ddot{\boldsymbol{u}} + t_m\rho_f\ddot{\boldsymbol{w}}) + \frac{\eta}{\kappa}\dot{\boldsymbol{w}}. \tag{40b}$$

where ψ_μ, ψ_{K_G}, $\psi_{\alpha M}$, and ψ_M are the relaxation functions of $\bar{\mu}$, $\bar{K}_G$, $\bar{\alpha}\bar{M}$, and $\bar{M}$, respectively. $\bar{K}_G$, $\bar{\alpha}\bar{M}$ and $\bar{M}$ are the functions of the new viscoelastic matrix bulk modulus $K_{unified}$. Therefore, their relaxation functions have the same form as Eq. (39), and these functions are presented in Appendix C, online. The viscoelastic matrix shear modulus $\bar{\mu}$ is provided by Carcione and Gurevich [56] and corresponds to the Zener model. Therefore, ψ_μ has the same form as the relaxation function of the Zener model, the details are also presented in Appendix C, online.

4. Applications to experimental data

4.1. Fully saturated tight sandstone

We use several groups of experimental data provided by Yin et al. [8] to examine the validity of the new model. The core used in the experiment is drilled from a tight sandstone reservoir in the northeastern Sichuan basin in China. The core has a porosity of 9% and a permeability of 0.063 mD. The bulk and shear moduli of the matrix materials are 40.32 and 40.69 GPa, respectively. Yin et al. [8] measured the wave velocities at both the dry and brine fully-saturated conditions at different effective pressures for a wide frequency range. The low-frequency measurements were conducted at [2, 200] Hz and the ultrasonic measurements were conducted at 1 MHz. The stiff and compliant porosities were also measured and they are dependent on the effective pressure. The aspect ratio α_m and the modified bulk modulus K_h are dependent on pressure. Based on the definition of K_h given by Mavko and Jizba [28] and Ref. [57], K_h should be large at a high pressure. And the aspect ratio should be low at a high pressure. Yin et al. [8] used 5.5×10^{-4} for the value of α_m. Since the experimental data does not contain the pressure-dependent α_m and K_h, we choose their values in a reasonable range. With the increase in pressure, the aspect ratio should decrease according to the formula given by Walsh [58] and the characteristic frequency of the squirt-flow model decrease according to Eq. (13).

Yin et al. [8] provided all the properties needed in the squirt-flow model, they are listed in Table 1. However, since the new unified model combines the two mechanisms, we still need to provide the parameters for the mesoscopic heterogeneity, including the matrix properties of the two mesoscopic phases. As mentioned in Section 2.1, the presence of clay can cause clay squirt flow [39,40,59] because the clay is much softer than other materials, such as quartz. The mesoscopic flow squirts from the clay phase to the stiff phase when the RVE is compressed. Yin et al. [8] provided a microscopic slice (3 mm diameter) of the core, which showed that the clay phase occurred at the mesoscopic scale. For this case, we choose the volume fraction of the soft phase as the volume fraction of clay (5.45%) and choose the scale of the mesoscopic heterogeneity L as 0.4 mm. The porosity of the RVE is the arithmetic mean of those of the two phases and the permeability and the matrix modulus are the harmonic means of those of the two phases, respectively [27]. The other physical properties are listed in Table 1.

We compute the velocity dispersion of the fast P-waves with the new poroviscoelastic model and compare the numerical results

Table 1
Properties used in the comparison between the experimental data [8] of the fully saturated tight sandstone and the numerical results calculated by new unified model.[a)]

	Phase 1	Phase 2	RVE
Brine viscosity (10^{-3} Pa s)	1.023	1.023	1.023
Brine bulk modulus (GPa)	2.28	2.28	2.28
Brine density (10^3 kg/m^3)	1013	1013	1013
Porosity (%)	8.44	20.6	8.94
Permeability (mD)	0.062	2.42	0.063
Rock material density (10^3 kg/m^3)	2.444	2.444	2.444
Rock material bulk modulus (GPa)	40.32	40.32	40.32
Rock material shear modulus (GPa)	40.69	40.69	40.69
Rock matrix bulk modulus (GPa)	13.4	6	12.8
Rock matrix shear modulus (GPa)	12.8	5.7	12.2
Volume fraction (%)	94.55	5.45	100
Tortuosity	–	–	2.4
Heterogeneity scale (mm)	–	–	0.4
Skempton's coefficient	0.626	0.587	0.591

[a)] "–" means that the property is not used in this study.

with the measured velocities. The results are shown in Fig. 3. In Fig. 3a, the stars represent the experimental data. The solid curves and the dashed curves are the predicted dispersions from our new unified model and the squirt-flow model, respectively. Fig. 3a shows that the new unified model provides a better fit of the experimental data than the squirt-flow model, especially at low effective pressure regime. We highlight the low-frequency measurement values with a dashed rectangle. We can observe that the characteristic frequency of the squirt-flow model is higher than the low-frequency measurement range for lower effective pressures. For example, at 2 MPa, the velocity dispersion of the squirt-flow model is not observed in the low-frequency measurement range (red dashed curve), which is inconsistent with the experimental data. However, in the result of our new unified model, we observe the dispersion caused by the mesoscopic heterogeneity in the low-frequency measurement range (solid curve). With the increase of the effective pressures, the characteristic frequency of the squirt-flow model decreases as the aspect ratio decrease. Therefore, we can observe the dispersion caused by the squirt-flow model in the low-frequency measurement range at high pressures. In Fig. 3b, the attenuations of the new unified model (red curve) and the squirt-flow model (red dashed curve) at 2 MPa are compared. There are two attenuation peaks in the curve of the new unified model. Unlike the squirt-flow model, the new unified model describes the energy loss of the mesoscopic heterogeneity, resulting in a difference between solid and dashed curves in Fig. 3b.

4.2. Partially saturated tight dolomite

In this section, we use dispersion data of a partially saturated dolomite to examine the validity of our new model. The data was provided by PetroChina. The core is drilled from a tight dolomite reservoir in the Sulige gas field. The core has a porosity of 5.72% and a permeability of 1.612 mD. The bulk modulus and density are 100 GPa and 2.695×10^3 kg/m^3, respectively. The data contain wave velocities of the dry rock core and of the core partially saturated with water in a wide frequency range. The low-frequency measurements are conducted at [1, 1171] Hz and the ultrasonic measurements are conducted at 600 kHz. The sample is 90% saturated with water and 10% saturated with air. We calculate the static elastic moduli of the dry matrix based on the velocities of the dry matrix. Since the experimental data do not contain α_m and K_h, we choose their values in a reasonable range. The properties are listed in Table 2. The volume fractions of the two phases are equal to the saturation of the fluids. The expressions of the unre-

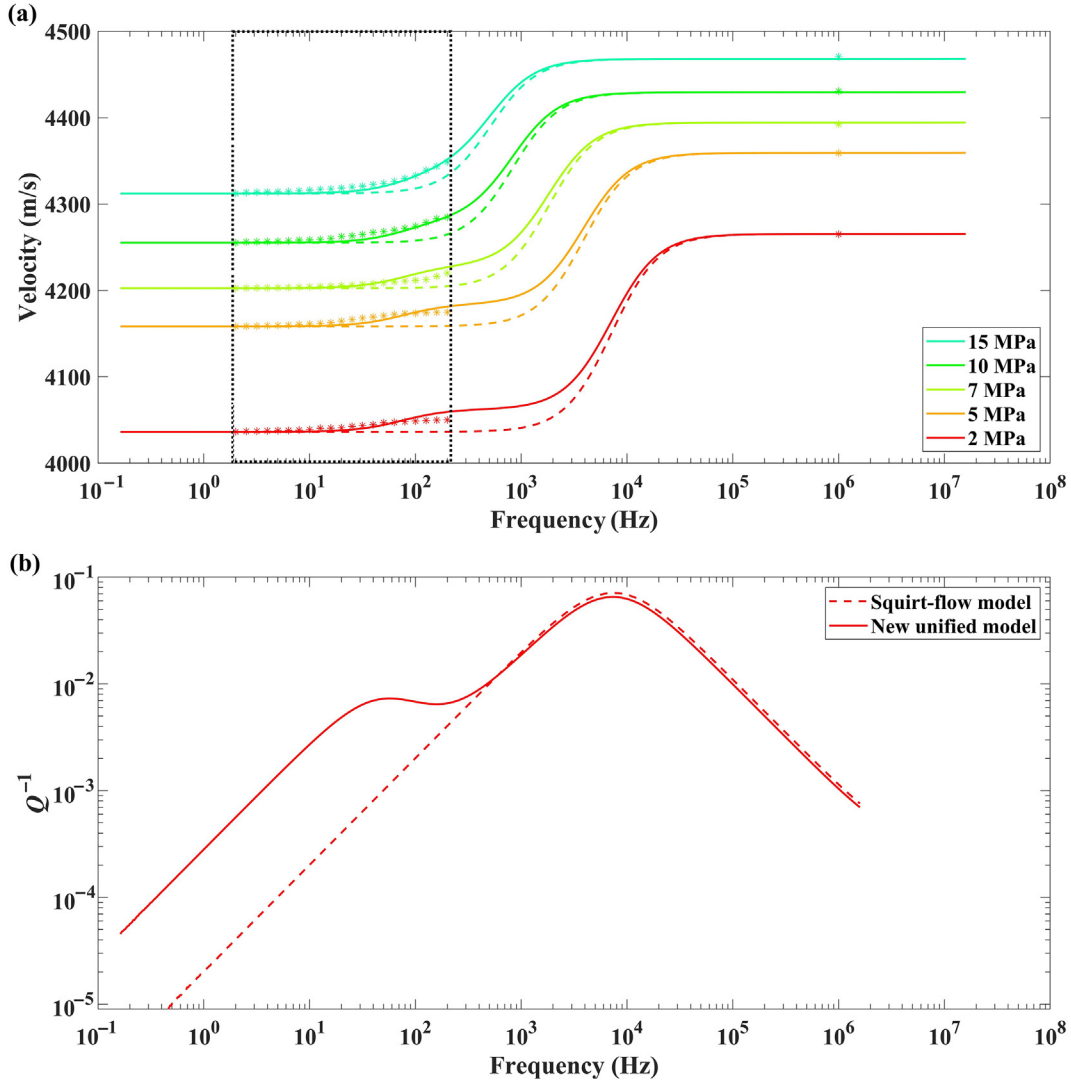

Fig. 3. Comparison of the experimental data (star markers) of the fully saturated tight sandstone, the numerical results calculated by the new unified model (solid curves) and the squirt-flow model (dashed curves). (a) P-wave phase velocities for brine; (b) P-wave inverse quality factor for the 2 MPa pressure.

Table 2
Properties used in the comparison between the experimental data of the partially saturated tight dolomite and the numerical results calculated by the new unified model.[a)]

	Phase 1	Phase 2	RVE
Fluids viscosity (10^{-3} Pa s)	0.89	0.01	0.57
Fluids bulk moduli (GPa)	2.38	1.418×10^{-6}	1.419×10^{-6}
Fluids densities (10^3 kg/m^3)	0.914	0.001	0.833
Porosity (%)	5.72	5.72	5.72
Permeability (mD)	1.612	1.612	1.612
Rock material density (10^3 kg/m^3)	2.695	2.695	2.695
Rock material bulk modulus (GPa)	100	100	100
Rock matrix bulk modulus (GPa)	44	44	44
Rock matrix shear modulus (GPa)	34	34	34
Water saturation (%)	–	–	90
Tortuosity	–	–	2.4
Heterogeneity scale (mm)	–	–	0.4
Skempton's coefficient	0.352	3.16×10^{-5}	3.15×10^{-4}

[a)] "–" means that the property is not used in this study.

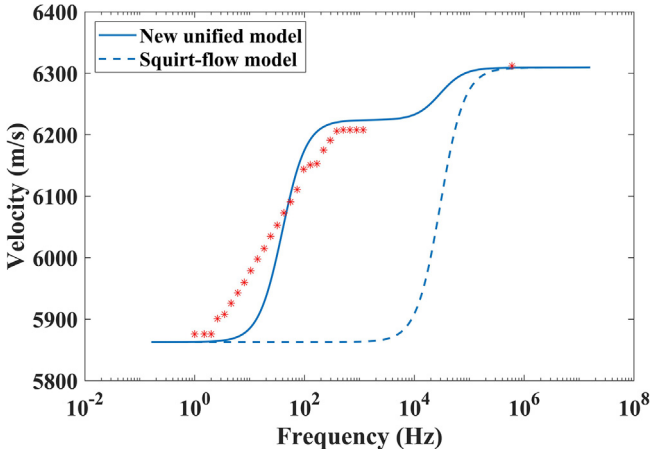

Fig. 4. Comparison of the experimental data (star markers) of the partially saturated tight dolomite, the numerical results calculated by the new unified model (solid curves) and the squirt-flow model (dashed curves): P-wave phase velocities.

laxed modulus are provided by Refs. [27,60] (see Appendix A online). We also choose 0.4 mm as the scale of the mesoscopic heterogeneity L.

We compute the velocity dispersion of the fast P-waves using the given physical properties and compare the numerical results with the measured velocities. The results are shown in Fig. 4, where the star markers represent the experimental data. The solid curves and the dashed curves are the numerical results calculated with the new unified model and the squirt-flow model, respectively. The results indicate that the experimental data has obvious dispersion in the low-frequency regime, and the velocity tends to constant around 1 kHz. The velocity at 600 kHz is much higher than the velocities around 1 kHz, which implies the occurrence of another transition between those two frequencies. The squirt-flow model cannot describe the dispersion in such a wide frequency regime. However, our new unified model provide a better fit than the squirt-flow model, which implies that the new model could be used to describe the dispersion caused by the patchy saturation and squirt-flow simultaneously.

5. Conclusions

In this study, we have described the characteristics of the dispersion and attenuation caused by mesoscopic and microscopic heterogeneities and proposed a new generalized Zener model with two modulus transitions and two attenuation peaks to combine the heterogeneities at two scales. The viscoelastic parameters in the new model are determined by the two mechanisms. We have also introduced the new viscoelastic model into the Biot poroelasticity theory to obtain new poroviscoelastic wave equations in the time and frequency domains. All the coefficients in our model have clear physical meanings and can be measured or estimated independently. We have compared the numerical results calculated with our new model with two groups of experimental data. One group comes from a fully saturated tight sandstone core and the other one comes from a partially saturated dolomite core. For tight porous rock saturated with fluid, the mesoscopic heterogeneity of the rock fabric and the microscopic heterogeneity of the pores are the two main mechanisms causing energy loss. For the partially saturated tight porous rock, energy loss is caused by the mesoscopic heterogeneity of fluid distribution and microscopic heterogeneity. The comparisons have shown that our new model can be used to describe the dispersion of waves. Since the new model unifies different mechanisms, it can be used for different types of data obtained in multi-frequency ranges, especially in the seismic frequencies.

Conflict of interest

The authors declare that they have no conflict of interest.

Acknowledgments

This work was supported by the National Natural Science Foundation of China (41390452, 91730306). The authors thank the Exploration and Development Research Institute of PetroChina Changqing Oilfield Company for providing the experimental data.

Author contributions

Boya Zhang and Dinghui Yang conceived the idea and developed the model. Boya Zhang performed the numerical experiments. Yuanfeng Cheng and Yunyin Zhang analyzed the data and participated in discussions. Boya Zhang and Dinghui Yang wrote the manuscript.

Appendix A–C. Supplementary data

Supplementary data to this article can be found online at https://doi.org/10.1016/j.scib.2019.05.027.

References

[1] Wang J, Yang D, Jing H, et al. Full waveform inversion based on the ensemble Kalman filter method using uniform sampling without replacement. Sci Bull 2019;64:321–30.
[2] Chen Y, Hu J, Peng F. Seismological challenges in earthquake hazard reductions: reflections on the 2008 Wenchuan earthquake. Sci Bull 2018;63:1159–66.
[3] Fang Z, Yang D. Inversion of reservoir porosity, saturation, and permeability based on a robust hybrid genetic algorithm. Geophysics 2016;80:R265–80.
[4] Pan X, Zhang G, Yin X. Azimuthally pre-stack seismic inversion for orthorhombic anisotropy driven by rock physics. Sci China Earth Sci 2018;61:425–40.
[5] Batzle ML, Han DH, Hofmann R. Fluid mobility and frequency-dependent seismic velocity—direct measurements. Geophysics 2006;71:N1–9.
[6] Tisato N, Quintal B, Chapman S, et al. Bubbles attenuate elastic waves at seismic frequencies: First experimental evidence. Geophys Res Lett 2015;42:3880–7.
[7] Pimienta L, Fortin J, Guéguen Y. Bulk modulus dispersion and attenuation in sandstones. Geophysics 2015;80:D111–27.
[8] Yin H, Zhao J, Tang G, et al. Pressure and fluid effect on frequency-dependent elastic moduli in fully saturated tight sandstone. J Geophys Res: Solid Earth 2017;122:8925–42.

[9] Müller TM, Gurevich B, Lebedev M. Seismic wave attenuation and dispersion resulting from wave-induced flow in porous rocks—a review. Geophysics 2010;75:75A147–64.
[10] Biot MA. Theory of propagation of elastic waves in a fluid-saturated porous solid. I. Low-frequency range. J Acoust Soc Am 1956;28:168–78.
[11] Biot MA. Theory of propagation of elastic waves in a fluid-saturated porous solid. II. Higher frequency range. J Acoust Soc Am 1956;28:179–91.
[12] Biot MA. Mechanics of deformation and acoustic propagation in porous media. J Appl Phys 1962;33:1482–98.
[13] Carcione JM. Wave fields in real media: wave propagation in anisotropic, anelastic, porous and electromagnetic media. 3rd ed. New York: Elsevier; 2014.
[14] White J. Computed seismic speeds and attenuation in rocks with partial gas saturation. Geophysics 1975;40:224–32.
[15] Pride SR, Berryman JG. Linear dynamics of double-porosity dual-permeability materials. I. Governing equations and acoustic attenuation. Phys Rev E 2003;68:036603.
[16] Pride SR, Berryman JG. Linear dynamics of double-porosity dual-permeability materials. II. Fluid transport equations. Phys Rev E 2003;68:036604.
[17] Ba J, Carcione J, Nie J. Biot-Rayleigh theory of wave propagation in double-porosity media. J Geophys Res 2011;116:B06202.
[18] Mavko G, Nur A. Melt squirt in the asthenosphere. J Geophys Res 1975;80:1444–8.
[19] Dvorkin J, Nur A. Dynamic poroelasticity: a unified model with the squirt and the Biot mechanisms. Geophysics 1993;58:524–33.
[20] Parra JO. The transversely isotropic poroelastic wave equation including the Biot and the squirt mechanisms: theory and application. Geophysics 1997;62:309–18.
[21] Yang D, Zhang Z. Effects of the Biot and the squirt-flow coupling interaction on anisotropic elastic waves. Chin Sci Bull 2000;45:2130–8.
[22] Cheng YF, Yang DH, Yang HZ. Biot/squirt model in viscoelastic porous media. Chin Phys Lett 2002;19:445.
[23] Yang D, Zhang Z. Poroelastic wave equation including the Biot/squirt mechanism and the solid/fluid coupling anisotropy. Wave Motion 2002;35:223–45.
[24] Nie J, Yang D, Yang H. A generalized viscoelastic Biot/squirt model for clay-bearing sandstones in a wide range of permeabilities. Appl Geophys 2009;5:249.
[25] Gurevich B, Makarynska D, de Paula OB, et al. A simple model for squirt-flow dispersion and attenuation in fluid-saturated granular rocks. Geophysics 2010;75:N109–20.
[26] Yang L, Yang D, Nie J. Wave dispersion and attenuation in viscoelastic isotropic media containing multiphase flow and its application. Sci China Phys Mech Astron 2014;57:1068–77.
[27] Pride SR, Berryman JG, Harris JM. Seismic attenuation due to wave-induced flow. J Geophys Res: Solid Earth 2004;109:B01201.
[28] Mavko G, Jizba D. Estimating grain-scale fluid effects on velocity dispersion in rocks. Geophysics 1991;56:1940–9.
[29] Gurevich B, Makarynska D, Pervukhina M. Ultrasonic moduli for fluid-saturated rocks: Mavko-Jizba relations rederived and generalized. Geophysics 2009;74:N25–30.
[30] Desbois G, Urai JL, Kukla PA, et al. High-resolution 3D fabric and porosity model in a tight gas sandstone reservoir: a new approach to investigate microstructures from mm-to nm-scale combining argon beam cross-sectioning and SEM imaging. J Pet Sci Eng 2011;78:243–57.
[31] Shah SM, Gray F, Crawshaw JP, et al. Micro-computed tomography pore-scale study of flow in porous media: effect of voxel resolution. Adv Water Resour 2016;95:276–87.
[32] Mavko G, Mukerji T, Dvorkin J. The rock physics handbook: tools for seismic analysis of porous media. 2nd ed. Cambridge: Cambridge University Press; 2009.
[33] Pimienta L, Borgomano JV, Fortin J, et al. Elastic dispersion and attenuation in fully saturated sandstones: role of mineral content, porosity, and pressures. J Geophys Res: Solid Earth 2017;122:9950–65.
[34] Rubino JG, Holliger K. Research note: seismic attenuation due to wave-induced fluid flow at microscopic and mesoscopic scales. Geophys Prospect 2013;61:882–9.
[35] Bachrach R. High resolution shallow seismic subsurface characterization Ph.D. thesis. Stanford: Stanford University; 1998.
[36] Carcione JM. Viscoelastic effective rheologies for modelling wave propagation in porous media. Geophys Prospect 1998;46:249–70.
[37] Zener C. Elasticity and anelasticity of metals. Chicago: University of Chicago Press; 1948.
[38] Liu X, Greenhalgh S, Zhou B, et al. Generalized poroviscoelastic model based on effective Biot theory and its application to borehole guided wave analysis. Geophys J Int 2016;207:1472–83.
[39] Best A, McCann C. Seismic attenuation and pore-fluid viscosity in clay-rich reservoir sandstones. Geophysics 1995;60:1386–97.
[40] Ba J, Zhao J, Carcione JM, et al. Compressional wave dispersion due to rock matrix stiffening by clay squirt flow. Geophys Res Lett 2016;43:6186–95.
[41] Johnson DL. Theory of frequency dependent acoustics in patchy-saturated porous media. J Acoust Soc Am 2001;110:682–94.
[42] Ba J, Xu W, Fu LY, et al. Rock anelasticity due to patchy saturation and fabric heterogeneity: a double double-porosity model of wave propagation. J Geophys Res: Solid Earth 2017;122:1949–76.
[43] Chapman S, Tisato N, Quintal B, et al. Seismic attenuation in partially saturated Berea sandstone submitted to a range of confining pressures. J Geophys Res: Solid Earth 2016;121:1664–76.
[44] Chapman S, Quintal B, Tisato N, et al. Frequency scaling of seismic attenuation in rocks saturated with two fluid phases. Geophys J Int 2017;208:221–5.
[45] Szewczyk D, Bauer A, Holt RM. Stress-dependent elastic properties of shales—laboratory experiments at seismic and ultrasonic frequencies. Geophys J Int 2017;212:189–210.
[46] Spencer JW, Shine J. Seismic wave attenuation and modulus dispersion in sandstones. Geophysics 2016;81:D211–31.
[47] Batzle ML, Kumar G, Hofmann R, et al. Seismic-frequency loss mechanisms: direct observation. Lead Edge 2014;33:656–62.
[48] Nowick AS, Berry BS. Anelastic relaxation in crystalline solids. London: Academic Press; 1972.
[49] Cole KS, Cole RH. Dispersion and absorption in dielectrics. I. Alternating current characteristics. J Chem Phys 1941;9:341–51.
[50] Liu X, Greenhalgh S, Zhou B, et al. Effective Biot theory and its generalization to poroviscoelastic models. Geophys J Int 2017;212:1255–73.
[51] Pimienta L, Sarout J, Esteban L, et al. Pressure-dependent elastic and transport properties of porous and permeable rocks: microstructural control. J Geophys Res: Solid Earth 2017;122:8952–68.
[52] Pride SR, Harris JM, Johnson DL, et al. Permeability dependence of seismic amplitudes. Lead Edge 2003;22:518–25.
[53] Jones TD. Pore fluids and frequency-dependent wave propagation in rocks. Geophysics 1986;51:1939–53.
[54] Biot MA, Willis DG. The elastic coefficients of the theory of consolidation. J Appl Mech 1957;24:594–601.
[55] Picotti S, Carcione JM. Numerical simulation of wave-induced fluid flow seismic attenuation based on the Cole-Cole model. J Acoust Soc Am. 2017;142:134–45.
[56] Carcione JM, Gurevich B. Differential form and numerical implementation of Biot's poroelasticity equations with squirt dissipation. Geophysics 2011;76:N55–64.
[57] Shapiro SA. Elastic piezosensitivity of porous and fractured rocks. Geophysics 2003;68:482–6.
[58] Walsh JB. The effect of cracks on the compressibility of rock. J Geophys Res 1965;70:381–9.
[59] Best AI, Priest JA, Clayton CRI, et al. The effect of methane hydrate morphology and water saturation on seismic wave attenuation in sand under shallow sub-seafloor conditions. Earth Planet Sci Lett 2013;368:78–87.
[60] Hill R. Elastic properties of reinforced solids: some theoretical principles. J Mech Phys Solids 1963;11:357–72.

Boya Zhang is currently a Ph.D. candidate under the supervision of Prof. Dinghui Yang in Department of Mathematical Sciences, Tsinghua University, where he received Bachelor's degree in 2014. His primary research focuses on reservoir geophysics.

Dinghui Yang is a professor of Department of Mathematical Sciences, Tsinghua University. His research interests include computational geophysics, seismic wave propagation and seismic tomography, seismic exploration, and reservoir geophysics.